Cite this: *J. Mater. Chem. A*, 2019, 7, 5748

Nb-Doped titanium phosphate for sodium storage: electrochemical performance and structural insights†

Natalia Voronina, Jae Hyeon Jo, Ji Ung Choi,  Chang-Heum Jo, Jongsoon Kim  and Seung-Taek Myung *

The effect of Nb⁵⁺ doping on the electrochemical and structural characteristics of NaTi₂(PO₄)₃ was investigated. The Nb⁵⁺ substitution lowered the band gap energy from 2.8 to 1.4 eV according to density functional theory calculations. Subsequent carbonization of pitch carbon on the surface of NaNb_xTi_{2-x}(PO₄)₃ ($x = 0.05$) significantly increased the electrical conductivity, thereby improving the capacity and high-rate capability. The excellent cyclability and superior electrode performance result from facile Na⁺ insertion and extraction that occur *via* a biphasic redox mechanism, namely, the Ti^{4+/3+} redox couple for the cathode and a sequence of two biphasic redox reactions associated with the Ti^{3+/2+} redox couple for the anode, as revealed by *operando* X-ray diffraction and *ex situ* X-ray absorption spectroscopic studies. Moreover, the possibility of application of Na_{2.9}Nb_{0.05}Ti_{1.95}(PO₄)₃ as both a cathode and anode material was demonstrated in a symmetric cell, which delivered a capacity of 105 mA h g⁻¹ after 100 cycles at 0.2C with a capacity retention of 83%.

Received 30th November 2018
Accepted 3rd February 2019

DOI: 10.1039/c8ta11517f

rsc.li/materials-a

Introduction

The last couple of decades have witnessed an increasing demand for large-scale batteries for energy storage systems. To meet the growing demand for energy storage, the development of alternative batteries and electrode materials has become extremely important. More significantly, the price and safety of new types of batteries are the most crucial elements for their further commercialization success. Rechargeable sodium ion batteries (SIBs) with titanium-based electrodes have recently attracted increasing attention because of their material abundance, low cost, efficient storage activity, chemical durability, and nontoxicity.^{1,2} On the anode side, the titanium redox provides a suitable insertion potential and superior structural stability, thereby ensuring the safety and long-term operation of SIBs.³⁻⁸ In addition, on the cathode side, titanium incorporated into layered structures plays an important role in stabilizing the two-dimensional structures of layered Na/Ti-containing oxides, adjusting the electrochemical potential, smoothening the voltage profiles, and extending the cycle life.⁹⁻¹¹

Among all titanium-based electrode materials for SIBs, Na superionic conductor (NASICON)-type NaTi₂(PO₄)₃ has attracted significant interest because of its unique structure. In the NASICON framework, TiO₆ octahedra are connected by corner-sharing PO₄ tetrahedra, forming an open structure with some vacant sites for sodium ions, which allow ultrafast and stable Na⁺ intercalation/extraction. NaTi₂(PO₄)₃ was first reported as an electrode material for SIBs in 1987 by Delmas *et al.*;¹² it was characterized by a flat voltage plateau at ~2.1 V *vs.* Na⁺/Na, attributed to the Ti^{4+/3+} redox. A recent revisit of NaTi₂(PO₄)₃ by Palacín *et al.*¹³ revealed the existence of an additional low-voltage plateau at ~0.4 V, which was attributed to the reduction of Ti³⁺ to Ti²⁺. According to this work, the redox reaction occurring at 2.1 V represents the phase transformation between NaTi₂(PO₄)₃ and Na₃Ti₂(PO₄)₃ (Ti^{4+/3+}), whereas the voltage plateau at 0.4 V reflects the transformation between Na₃Ti₂(PO₄)₃ and Na₄Ti₂(PO₄)₃ (Ti^{3+/2+}).

NaTi₂(PO₄)₃ has a large band gap, resulting in a very low electronic conductivity¹⁴ and thus leading to unsatisfactory cycling performance. Recently, several approaches have been proposed to improve its electrochemical properties, namely, particle size reduction accompanied by carbon coating to shorten the electron and ion diffusion distances, which is intended to increase the electronic conductivity and enhance the rate performance. Surface modifications using electroconductive layers, such as porous carbon, graphene, and carbon nanotubes and nanofibers, together with nanostructuring such as the use of hierarchicalization and mesoporous nano-assemblies have been implemented as promising methods to

Department of Nano Technology and Advanced Materials Engineering, Sejong Battery Institute, Sejong University, Seoul, 05006, South Korea. E-mail: smyung@sejong.ac.kr

† Electronic supplementary information (ESI) available: Rietveld refinement results (NTP, NTP-C, NNbTP and NNbTP-C powders, and NTP-C and NNbTP-C electrodes at different states of discharge/charge and after long term cycling), Raman spectroscopy, SEM, impedance results, charge/discharge profiles of Super P-pitch carbon, and TEM image and the corresponding SAED pattern of NTP-C. See DOI: 10.1039/c8ta11517f

improve the electrode performance of $\text{NaTi}_2(\text{PO}_4)_3$.^{15–21} Specifically, nanosized $\text{NaTi}_2(\text{PO}_4)_3$ anchored on reduced graphene $\text{NaTi}_2(\text{PO}_4)_3/\text{rGO}$ displayed good electrochemical performance as an anode, delivering a high reversible capacity of 130 mA h g^{-1} at 0.1C with high rate capability and long stable cyclability.¹⁵

However, nanotexturing of active materials is not likely to be favored for large-scale production because of the high cost and difficulty of implementation. Several earlier studies suggested significant improvement in electrochemical performances by partial replacement of Ti^{4+} by pentavalent ions such as Nb^{5+} and Ta^{5+} in $\text{Li}_4\text{M}_x\text{Ti}_{5-x}\text{O}_{12}$ (M: Nb and Ta),^{22,23} which resulted in the formation of some Ti^{3+} for charge compensation in the oxide matrix. A similar effect has been seen in Nb^{5+} -doped $\text{Nb}_x\text{Ti}_{1-x}\text{O}_2$.²⁴ Also, we experimentally proved that the presence of Ti^{3+} in TiO_2 increases the resulting electrical conductivity to facilitate improvement of electrode performances.²⁵ Using this concept, it should also be possible to modify the intrinsically low electrical conductivity of NASICON-type electrode materials such as $\text{Li}_3\text{V}_2(\text{PO}_4)_3$, $\text{Na}_3\text{V}_2(\text{PO}_4)_3$ and $\text{NaTi}_2(\text{PO}_4)_3$. Transition metal ions such as Mn, Cr, Co, Fe, and Mo have previously been introduced into $\text{Li}_3\text{V}_2(\text{PO}_4)_3$ and $\text{Na}_3\text{V}_2(\text{PO}_4)_3$ compounds.^{26–32} The replacement of Ti by several aliovalent elements such as Al, Fe, and Nb has also been achieved and resulted in improved cycling stability of $\text{NaTi}_2(\text{PO}_4)_3$.^{33–36}

Herein, Nb^{5+} was used as a dopant to modify the properties of $\text{NaTi}_2(\text{PO}_4)_3$. Nb^{5+} is a typical transition metal ion with a radius of 0.64 Å, which is slightly larger than that of Ti^{4+} (0.605 Å). The formation of a thin layer of pitch carbon together with introduction of the aliovalent dopant can dramatically increase the electrical conductivity in both the bulk and surface. The use of carbon-coated Nb^{5+} -doped titanium phosphate as both the cathode and anode material resulted in excellent structural stability and outstanding rate capability.

The Na-storage mechanism was also investigated in carbon-coated $\text{NaNb}_{0.05}\text{Ti}_{1.95}(\text{PO}_4)_3$ using *operando* X-ray diffraction (XRD) and *ex situ* X-ray absorption near edge spectroscopy studies. Sodium ions were shown to reversibly migrate into and out of the host structure *via* a biphasic redox mechanism involving the $\text{Ti}^{4+/3+}$ redox couple at 2.1 V *vs.* Na^+/Na and a $\text{Ti}^{3+/2+}$ redox pair associated with two biphasic reactions at 0.4 V *vs.* Na^+/Na . Moreover, the carbon-coated $\text{NaNb}_{0.05}\text{Ti}_{1.95}(\text{PO}_4)_3//$ carbon-coated $\text{NaNb}_{0.05}\text{Ti}_{1.95}(\text{PO}_4)_3$ symmetric cell exhibited zero-strain characteristics because of the inversed volume changes of the cathode and the anode during charge and discharge, leading to excellent cycling performance (105 mA h g^{-1} after 100 cycles at 0.2C, 83% capacity retention) and flexibility for practical applications.

Experimental

Synthesis of materials

The co-precipitation method was used to prepare the $\text{NaNb}_x\text{Ti}_{2-x}(\text{PO}_4)_3$ ($x = 0; 0.05$) materials. First, $\text{Ti}(\text{OC}_2\text{H}_5)_4$ (Aldrich) was dissolved in ethanol. In a separate beaker, $\text{NH}_4\text{H}_2\text{PO}_4$ (Samchun) and NaNO_3 (Samchun) were dissolved in water. After complete mixing of the two solutions, NbCl_5 was added. The molar ratio of the precursors was $\text{Na} : \text{Ti}_{2-x} : \text{Nb}_x : \text{P} = 1 : 2 - x : x : 3$. This

final solution was then mixed at room temperature for 1 h. Following the evaporation of the solvent on a hot plate at 100 °C, the mixture was dried in a convection oven at 120 °C. The obtained powders were subsequently calcined at 900 °C in air for 6 h and naturally cooled to room temperature. These powders were denoted as NTP and NNbTP, respectively. Next, 10 g of each powder was mixed with pitch carbon and further heat-treated at 750 °C for 2 h in an Ar atmosphere to obtain carbon-coated NTP (NTP-C) and carbon-coated NNbTP (NNbTP-C).

Characterization

XRD (PANalytical, X'Pert) was used to investigate the crystal structure of the samples. The XRD data were obtained in the 2θ range of 10–80° using a step size of 0.03°. The FULLPROF program³⁷ was used to refine the recorded XRD patterns of the NTP, NNbTP, NTP-C, and NNbTP-C powders and electrodes. The morphologies of the obtained powders were examined using scanning electron microscopy (SEM; JXA-8100, JEOL) and high-resolution transmission electron microscopy (HR-TEM; H-800, Hitachi). The compositions of the synthesized materials were analyzed by ICP-atomic emission spectroscopy (ICP-AES, OPTIMA 8300, Perkin-Elmer). The electrical conductivities of NTP, NNbTP, NTP-C, and NNbTP-C were measured using the direct volt-ampere method (CMT-SR1000, AIT) using the four-point probe technique. Raman spectra were obtained in the region of 200–3000 cm^{-1} using Raman spectroscopy (inVia, Renishaw). The amount of carbon in the materials was determined using an elemental analyzer (EA110, CE Instruments). Structural studies during cycling were carried out using *operando* XRD (PANalytical, X'Pert) and *ex situ* X-ray absorption near-edge structure (XANES) spectroscopy. The XANES measurements were performed at the 8C beamline of the Pohang Accelerator Laboratory (PAL), Pohang, South Korea, and the data were analyzed using the Athena software package.³⁸

Electrochemical tests

For electrode fabrication, the synthesized NTP, NNbTP, NTP-C, and NNbTP-C were mixed with a conducting agent (Super P) and polyvinylidene fluoride (PVDF) at a weight ratio of 8 : 1 : 1 in *N*-methyl-2-pyrrolidone (NMP) to form a homogeneous slurry. The slurry was applied onto Al foil and dried overnight at 120 °C under vacuum. The electrochemical properties of the products were evaluated using 2032 coin-type cells. The Na metal was used as the anode, Whatman GF/C glass fiber was used as the separator, and 0.5 M NaPF_6 solution in a 98 : 2 volume mixture of polyethylene carbonate (PC) and fluoroethylene carbonate (FEC) was used as the electrolyte. All the cells were prepared in an Ar-filled glove box with oxygen and moisture contents below 0.1 ppm. The cells were tested in galvanostatic mode at different current densities in the voltage ranges of 1.5–3 V and 0.01–1.5 V *vs.* Na^+/Na at 25 °C. Galvanostatic intermittent titration technique (GITT) measurements of the electrodes were conducted with 30 min charge or discharge and open-circuit periods of 1 h.

In order to see if the NNbTP-C material has the potential for industrial use as both the cathode and anode, the laminated-type full cell wrapped with an Al pouch was fabricated. The

electrode size of the full-cell was 3 cm × 5 cm. The cell was cycled between 1.2 and 2.6 V with a rate of 5C.

Computational details

First-principles calculations were performed to estimate the energies of the given materials based on the spin-polarized generalized gradient approximation (GGA) proposed by Perdew–Burke–Ernzerhof (PBE) using density functional theory (DFT).³⁹ We used a plane-wave basis set and the projector-augmented wave (PAW)⁴⁰ method implemented in the Vienna *ab initio* simulation package (VASP).⁴¹ PAW potentials have shown good predictive capability for cathode materials of various rechargeable batteries. The Hubbard U parameter (GGA + U)⁴² was added to correct for the self-interaction of GGA. A U_{eff} value for Ti of 4.2 eV was selected, which was previously determined from the self-consistent calculation of Nb-doped TiO₂.⁴³ A plane-wave basis with an energy cutoff of 500 eV was used. All the structures were optimized until the force in the unit cell converged to within 0.05 eV Å⁻¹.

Results and discussion

Material synthesis

To investigate the crystal structures of the pristine NTP, NNbTP, NTP-C, and NNbTP-C materials, Rietveld refinement of the XRD patterns was performed assuming the rhombohedral $R\bar{3}C$ space group (Fig. 1, Table S1 and Fig. S1, ESI†). The results indicate that Nb⁵⁺ incorporation and carbon coating do not alter the structure of NTP. As observed in Table S1,† compared with NTP and NTP-C, the Nb⁵⁺ doping in NNbTP and NNbTP-C resulted in slight increases in the unit cell volume due to the slightly larger ionic radius of Nb⁵⁺ (0.64 Å) than that of Ti⁴⁺ (0.605 Å), implying that the replacement of Ti⁴⁺ by Nb⁵⁺ was successful. Five batches of the as-synthesized NTP and NNbTP were measured by ICP-AES to determine the chemical compositions of both compounds. The analyzed chemical formulas of NTP and Nb-doped NTP are exhibited in average as follows: Na_{0.999}Ti_{1.000}(PO₄)₃ and Na_{0.992}Nb_{0.049}Ti_{1.951}(PO₄)₃. The resulting crystal structures of NTP-C and NNbTP-C are shown in the insets of Fig. 1a and b, respectively; the structures consist of TiO₆/NbO₆ octahedra and PO₄ tetrahedra, interlinked by corner sharing. Sodium ions occupy only interstitial sites with octahedral (M1) geometries.

The effect of Nb doping of NTP was verified using first-principles calculations. Using the structural information calculated from Rietveld refinement, we predicted the theoretical value of the band gaps of NTP and NNbTP. As shown in Fig. 1c and d, it was observed that with Nb⁵⁺ doping of NTP, a defect state in the band gap separated from the conduction band was generated, indicating that Nb⁵⁺ doping resulted in a decrease of the band gap of NTP. This result is similar to previous findings on the effect of Nb⁵⁺ doping on TiO₂.⁴³ Note that the average oxidation state of Ti for the NNbTP was slightly lower than that of the NTP in Fig. 1e. This indicates that the incorporation of Nb into the NTP structure induced the formation of Ti³⁺ in the crystal structure. The spectrum for Nb

in NNbTP overlaps with that for Nb₂O₅, suggesting that the oxidation state of Nb is close to that of Nb⁵⁺ after introduction into the Ti site (Fig. 1f). As mentioned in Fig. 1c and d, the observation of a new band gap at ~1.38 eV is likely due to the presence of Ti³⁺ induced by the incorporation of Nb⁵⁺ into NaNb_{0.05}Ti_{1.95}(PO₄)₃. More importantly, the increase in the electrical conductivity of the NNbTP is evidence of the presence of Ti³⁺ in the phosphate lattice (Table S1, ESI†). The electrical conductivities of NTP and NNbTP were ~7 × 10⁻⁶ and ~3 × 10⁻⁵ S cm⁻¹, respectively. Although the electrical conductivity was more improved by the larger amount of Nb introduced into NaNb_{0.1}Ti_{1.9}(PO₄)₃, ~5 × 10⁻⁵ S cm⁻¹ with a single phase (Fig. S2, ESI†), we excluded the composition for further investigation due to its low crystallinity that may affect poor capacity retention during the cycling test. As we mentioned in the Introduction, the mixed valence of Ti, Ti⁴⁺ as a majority together with a small amount of Ti³⁺, in the crystal structure is responsible for the reduction in the band gap energy and electrical conductivity. It is also notable that carbon coating increased the conductivity even more approximately 9 × 10⁻⁴ for NTP and 2 × 10⁻³ S cm⁻¹ for NNbTP. These high electrical conductivities are attributed not only to the Nb⁵⁺ doping but also to the presence of the uniformly distributed carbon layer on the surface of NTP and NNbTP derived from the pitch, as confirmed by the appearance of both D and G bands at 1350 and 1600 cm⁻¹ in the Raman spectra (Fig. S3, ESI†). The carbon content was approximately 6.25 wt% for both carbon-coated composites. The peaks observed between 800 and 1200 cm⁻¹ are typical peaks of NTP, which support the formation of a pure NTP phase. The peak positions did not vary with the substitution of Ti⁴⁺ by Nb⁵⁺.

The morphological and structural features of the NTP-C and NNbTP-C were characterized using SEM and TEM. As observed in the SEM images, the primary particle sizes of NTP and NNbTP ranged from 50 to 250 nm in diameter (Fig. S4, ESI†). Neither the primary particle size nor the particle size distribution noticeably changed after the Nb⁵⁺ doping. The TEM image shows that a uniform thin carbon coating layer with a thickness of approximately 2.5 nm grew on the surface of the particles. The selected area electron diffraction (SAED) patterns of NTP (Fig. 1g) and NNbTP-C (Fig. 1h) along the [001] zone axis confirm that there was no change in the symmetry after the surface modification with pitch carbon and Nb⁵⁺ doping. The TEM elemental energy-dispersive X-ray spectroscopy (EDX) results reveal that Na, Ti, Nb, P, and O were homogeneously distributed in the NNbTP sample (Fig. 1i).

Electrochemical performance in Na cells

The synthesized NTP, NNbTP, NTP-C, and NNbTP-C were tested in Na cells in the voltage range of 0.01–3 V at a rate of 0.2C (1C = 130 mA g⁻¹) (Fig. 2a). The discharge curves contain three distinct voltage plateaus: a long well-defined plateau at ~2.1 V, a sloppy plateau at ~1.25 V, and a flat plateau at ~0.4 V. The upper flat plateau observed at 2.1 V is associated with the Ti^{4+/3+} redox couple, which usually appears in the NASICON-type NTP material. However, this plateau was much shorter for the NTP and NNbTP materials than for the carbon-coated samples,

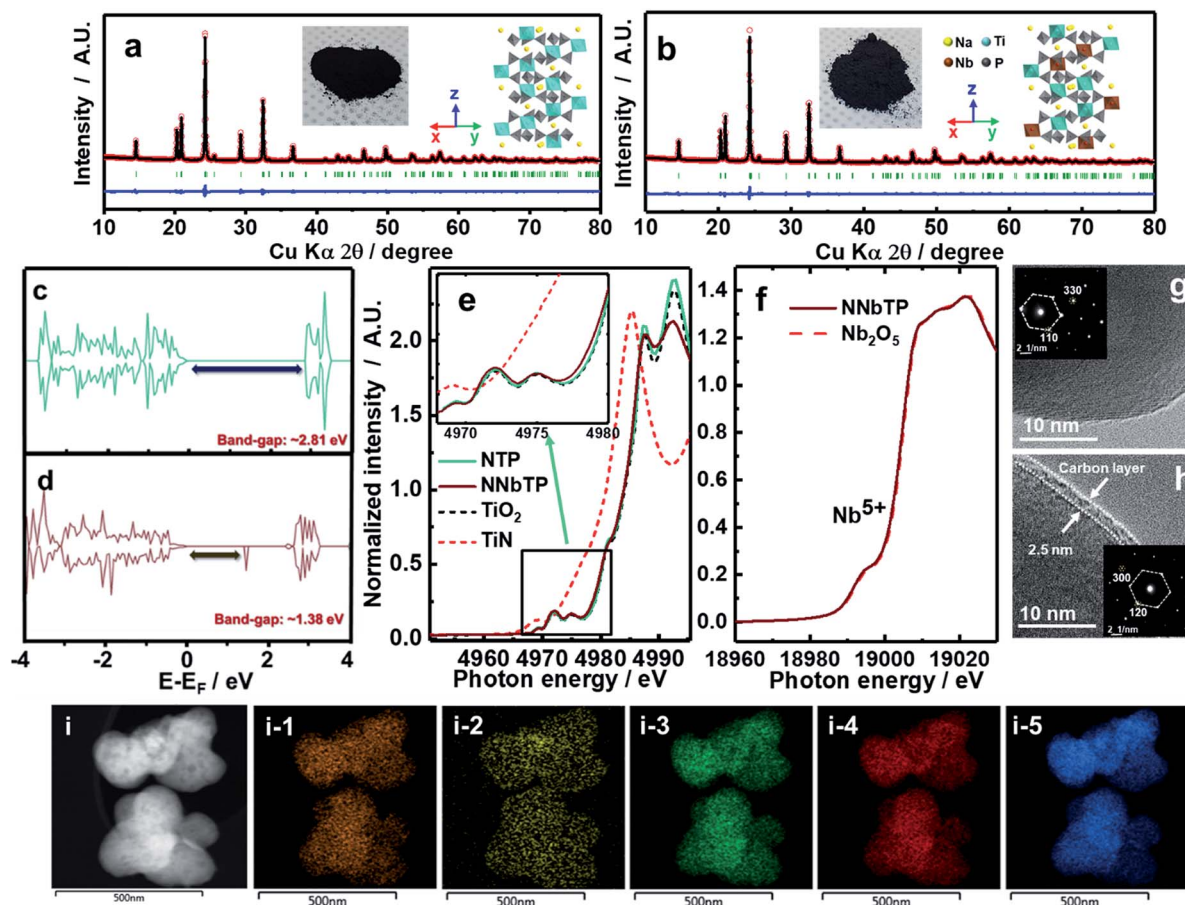


Fig. 1 Rietveld refinement of XRD patterns for (a) NTP-C (inset: digital image of the powder and crystal structure drawn based on refinement results presented in Table S1, ESI†) and (b) NNbTP-C. Band gap of (c) NTP and (d) NNbTP obtained from DFT calculations. (e) XANES K-edge spectra of Ti for NTP and NNbTP. (f) XANES K-edge spectra of Nb for NNbTP. TEM images of (g) NTP (inset: SAED pattern along the [001] zone axis) and (h) NNbTP-C (inset: SAED pattern along the [001] zone axis). (i) TEM image and the corresponding EDX mapping of NNbTP, (i-1) Na, (i-2) Nb, (i-3) Ti, (i-4) P, (i-5) O.

presumably because of the low electrical conductivity. The second sloppy plateau at 1.25 V is irreversible, which can likely be attributed to the formation of a solid-electrolyte interphase (SEI) layer and the irreversible reaction of sodium with amorphous carbon such as the added conducting carbon agent and

coating layers. Notably, the third two-step plateau at approximately 0.4 V vs. Na^+/Na was clearly observed only for the NTP-C and NNbTP-C electrodes and is attributed to the $\text{Ti}^{3+}/\text{Ti}^{2+}$ redox. The voltage profile was not reversible on charge for the bare NTP and NNbTP materials, as the feature of the two plateaus was not

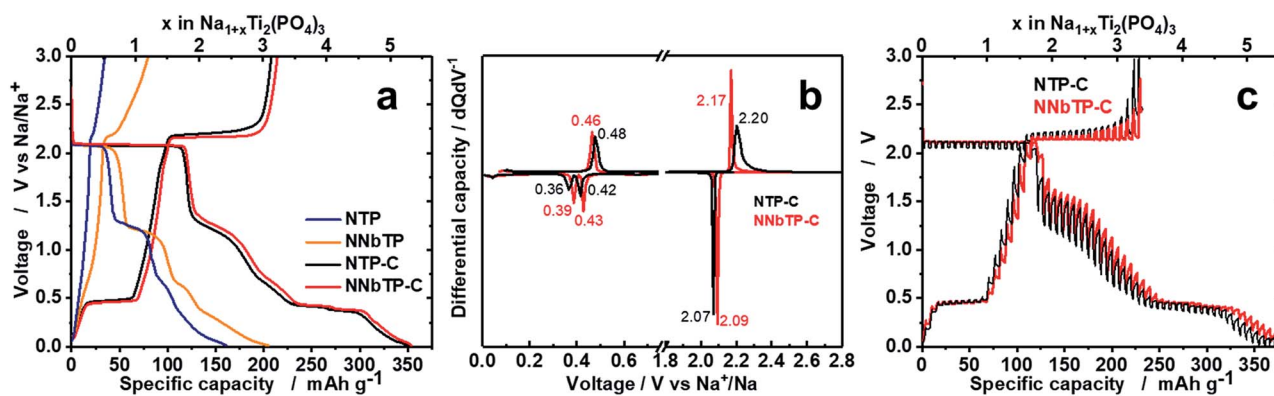


Fig. 2 (a) First discharge (reduction) and charge (oxidation) curves in the voltage range of 0.01–3 V: bare NTP (blue line), bare NNbTP (orange line), carbon-coated NTP-C (black line), and carbon-coated NNbTP-C (red line). (b) Resulting dQ/dV profiles of NTP-C and NNbTP-C. (c) GITT curves of NTP-C and NNbTP-C in the voltage range of 0.01–3 V at 0.1C.

observed. Surprisingly, the plateaus at 2.1 and 0.4 V were clearly observed on charge for the NTP-C and NNbTP-C electrodes. From the discharge profile and the dQ/dV curve (Fig. 2b), a low-voltage two-step plateau can be clearly resolved at 0.43 and 0.39 V for NNbTP-C (0.42 and 0.36 V for NTP-C); however, these plateaus merged into a one-step plateau on charge. Both the high-voltage (2.1 V vs. Na^+/Na) and low-voltage (0.4 V vs. Na^+/Na) two-step plateaus are quite flat, suggesting that these plateaus are associated with a two-phase reaction during the insertion of Na^+ ions.

Further experiments were performed using only the carbon-coated NTP-C and NNbTP-C electrodes because the samples without carbon coating exhibited unsatisfactory performance. As revealed in Fig. 2c, the voltage difference between charge and discharge was lower for the NNbTP-C electrode than that for the NTP-C electrode. To demonstrate that Nb^{5+} doping improves the kinetics, GITT measurements were performed at a scan rate of 0.1C with 30 min discharge or charge with an open-circuit period of 1 h. The relaxation spikes of the NTP-C electrode were elongated, indicating slower intercalation/deintercalation reaction kinetics with larger polarization and slower equilibration at both voltage plateaus. We compared the diffusion coefficients at $\text{Na}_{1.1}\text{Ti}_2(\text{PO}_4)_3$ and $\text{Na}_{1.1}\text{Nb}_{0.05}\text{Ti}_{1.95}(\text{PO}_4)_3$ compositions at a high-voltage plateau, where the sodium-poor $R\bar{3}C$ phase is dominant. The resulting diffusivities of $\text{Na}_{1.1}\text{Ti}_2(\text{PO}_4)_3$ and $\text{Na}_{1.1}\text{Nb}_{0.05}\text{Ti}_{1.95}(\text{PO}_4)_3$ are $1.76 \times 10^{-11} \text{ cm}^2 \text{ s}^{-1}$ and $4.35 \times 10^{-11} \text{ cm}^2 \text{ s}^{-1}$, respectively, on sodiation (discharge). On desodiation (charge), we also calculated the diffusion coefficients at the same compositions, $\text{Na}_{1.1}\text{Ti}_2(\text{PO}_4)_3$ and $\text{Na}_{1.1}\text{Nb}_{0.05}\text{Ti}_{1.95}(\text{PO}_4)_3$, namely, $5.02 \times 10^{-11} \text{ cm}^2 \text{ s}^{-1}$ and $8.92 \times 10^{-11} \text{ cm}^2 \text{ s}^{-1}$, respectively. The Nb^{5+} doping is evidently beneficial for the improvement of Na^+ diffusion, and the efficacy appears to be more significant on discharge because Na^+ diffusion occurs somehow slow during Na^+ insertion (discharge) into the structure. From the above results, the effect of Nb^{5+} inducing the formation of Ti^{3+} in $\text{NaNb}_{0.05}\text{Ti}_{1.95}(\text{PO}_4)_3$ appears more positively on the improvement of Na^+ diffusion.

The distinct voltage plateaus at 2.1 and 0.4 V urged us to test both NTP-C and NNbTP-C as cathodes between 1.5 and 3 V and as anodes between 0.01 and 1.5 V in a half-cell configuration. As shown in the inset of Fig. 3a, the NTP-C electrode delivered a capacity of $122.6 \text{ mA h g}^{-1}$ at 0.2C, which is lower than that of the doped NNbTP-C electrode ($125.3 \text{ mA h g}^{-1}$ at 0.2C). The cycle performances of the undoped and doped NTP-C and NNbTP-C electrodes at 0.2C are compared in Fig. 3a. It is evident that the NNbTP-C electrode exhibited higher capacity, although both electrodes showed a similar tendency for capacity retention, 92.6% and 95% over 100 cycles for NTP-C and NNbTP-C, respectively. Fig. 3b displays the rate performance of the NTP-C and NNbTP-C electrodes at different currents from 0.5C to 100C. It is clear that the NNbTP-C electrode provides better rate capability than the undoped NTP-C electrode, especially for the delivery of capacity at 100C (though the NTP-C did not have capacity over 70C). The capacities of both electrodes were restored to their initial values when the current returned to 1C after 100C (Fig. 3c). To test the longer cycling stability, NTP-C and NNbTP-C electrodes were tested at

5C and exhibited a markedly good capacity retention of 88% and 91% after 1000 cycles, respectively (Fig. 3d). Achieving good high-rate capabilities is challenging in SIBs because of the large size of Na^+ ions, which usually results in severe volume changes in the host materials.

Utilization of the $\text{Ti}^{3+/2+}$ redox couple in NASICON-type materials is beneficial for anode materials. Therefore, investigation of the structural stability of the low-voltage plateau is important. The charge-discharge profiles and the cycle life of NTP-C and NNbTP-C in the voltage range of 0.01–1.5 V at 0.2C are shown in Fig. 3e. NTP-C and NNbTP-C delivered reversible capacities of 82 and 86 mA h g^{-1} , respectively. In addition, the materials exhibited stable cycle performance, and the capacities were maintained at 65 and 73 mA h g^{-1} , respectively, for NTP-C and NNbTP-C after 100 cycles (Fig. 3e). Upon increasing the C-rate to 5C, NTP-C and NNbTP-C delivered capacities of 63 and 77 mA h g^{-1} , respectively (Fig. 3f and g). The capacities were also restored to their initial values when the electrodes were tested at 1C after application of 50C. Further cycling tests at 5C revealed acceptable levels of capacity retention over 1000 cycles, 72% for NTP-C and 78% for NNbTP-C (Fig. 3h).

The above electrochemical data demonstrate that both the cycling stability and power capability were affected by the Nb^{5+} doping, presumably attributed to the improved electrical conductivity of NNbTP-C compared with that of NTP-C. Notably, it is reported for the first time that the reversible capacity delivered on the lower plateau for long-term cycling over 1000 cycles confirms the structural stability of the present NASICON-type NNbTP-C electrode material.

Sodium insertion and extraction into/from $\text{NaNb}_{0.05}\text{Ti}_{1.95}(\text{PO}_4)_3\text{-C}$ (1.5–3 V)

Operando XRD measurements were performed for the NNbTP-C cell that was discharged and charged at 0.2C (Fig. 4a and b). Upon discharging, several new diffraction peaks gradually appeared at 20.1° , 23.6° , 28.5° , 31.1° , 32.0° , and 35.1° (2θ) (Fig. 4b). Their intensities became more intense whereas the diffraction peaks from the initial phase gradually decreased and disappeared upon further discharging, which is a typical feature of a biphasic reaction, consistent with the flat electrochemical plateau observed at 2.1 V. This leads to a phase transition from the sodium-poor $\text{NaNb}_{0.05}\text{Ti}_{1.95}(\text{PO}_4)_3$ ($R\bar{3}C$) phase to the sodium-rich $\text{Na}_{2.9}\text{Nb}_{0.05}\text{Ti}_{1.95}(\text{PO}_4)_3$ ($P\bar{1}$) phase. To prove the formation of $\text{Na}_{2.9}\text{Nb}_{0.05}\text{Ti}_{1.95}(\text{PO}_4)_3$ with the $P\bar{1}$ space group, Rietveld refinement was performed for the NNbTP-C electrode discharged to 1.5 V (Fig. 4c), and the results are summarized in Table S2, ESI.† The parameters of the refined XRD pattern matched well with those reported for $\text{Na}_3\text{Ti}_2(\text{PO}_4)_3$ by Palacín *et al.*¹³ It should be noted that 1.9 mol of sodium insertion corresponds to a change of approximately 7.5% in the unit cell volume with respect to that of the sodium-poor $\text{NaNb}_{0.05}\text{Ti}_{1.95}(\text{PO}_4)_3$ phase. During charge, peaks from $\text{NaNb}_{0.05}\text{Ti}_{1.95}(\text{PO}_4)_3$ appeared again, although they coexisted with those of the sodium-rich $\text{Na}_{2.9}\text{Nb}_{0.05}\text{Ti}_{1.95}(\text{PO}_4)_3$ phase. At the end of charge, the structure of the material was restored to that of the original $\text{NaNb}_{0.05}\text{Ti}_{1.95}(\text{PO}_4)_3$ (Fig. 4b), as evidenced by the Rietveld

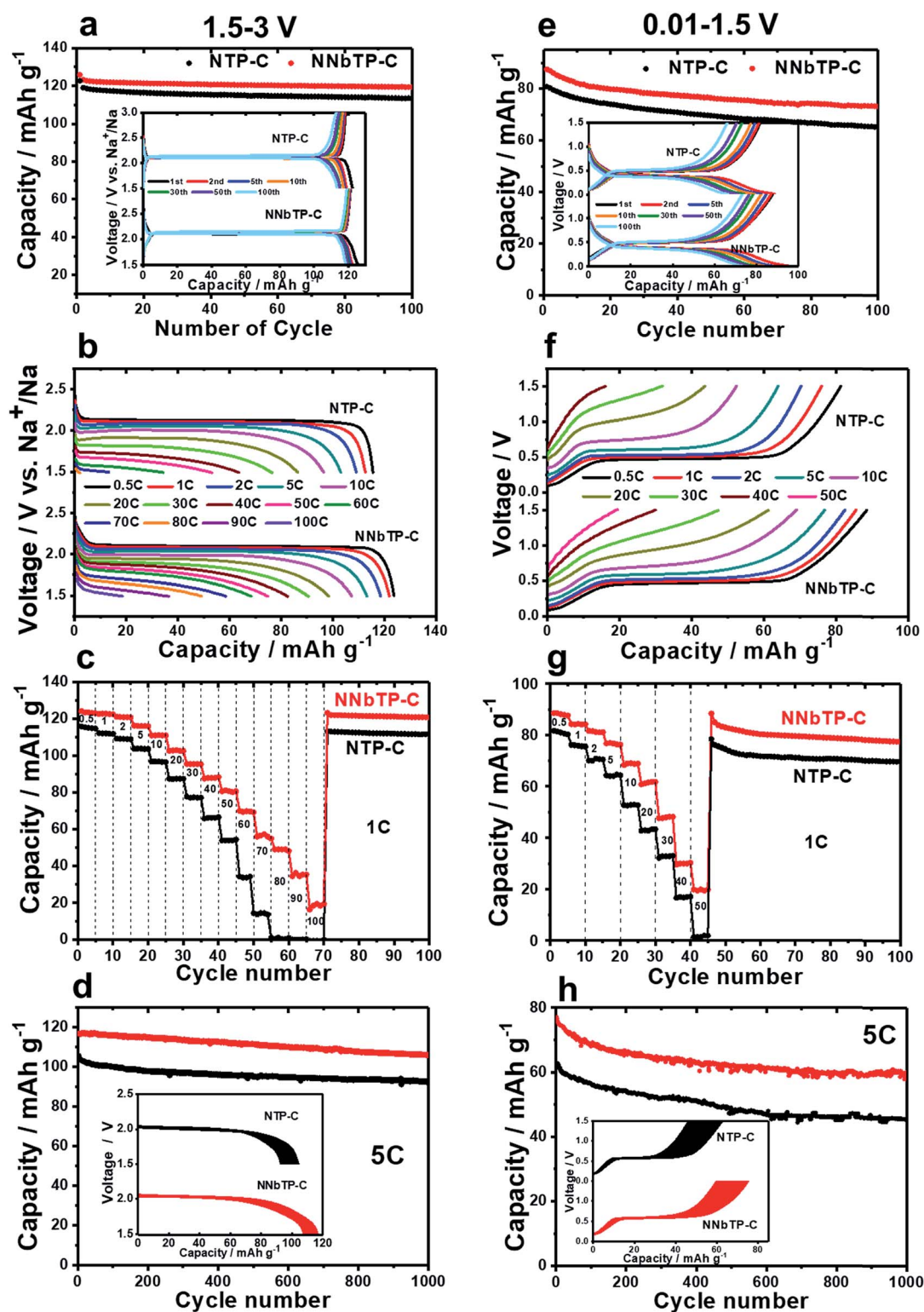


Fig. 3 Electrochemical performance of NTP-C and NNbTP-C in the voltage range of 1.5–3 V: (a) cycling performance and charge/discharge profiles of NTP-C and NNbTP-C at 0.2C, (b) discharge profiles at different currents of 0.5–100C, (c) cycling performance at different currents at 0.5–100C, and (d) cycling performance and discharge profiles of NTP-C and NNbTP-C at 5C. Electrochemical performance of NTP-C and NNbTP-C in the voltage range of 0.01–1.5 V. (e) cycling performance and charge/discharge profiles of NTP-C and NNbTP-C at 0.2C, (f) charge profiles at different currents at 0.5–50C, (g) cycling performance at different currents at 0.5–50C, and (h) cycling performance and discharge profiles of NTP-C and NNbTP-C at 5C.

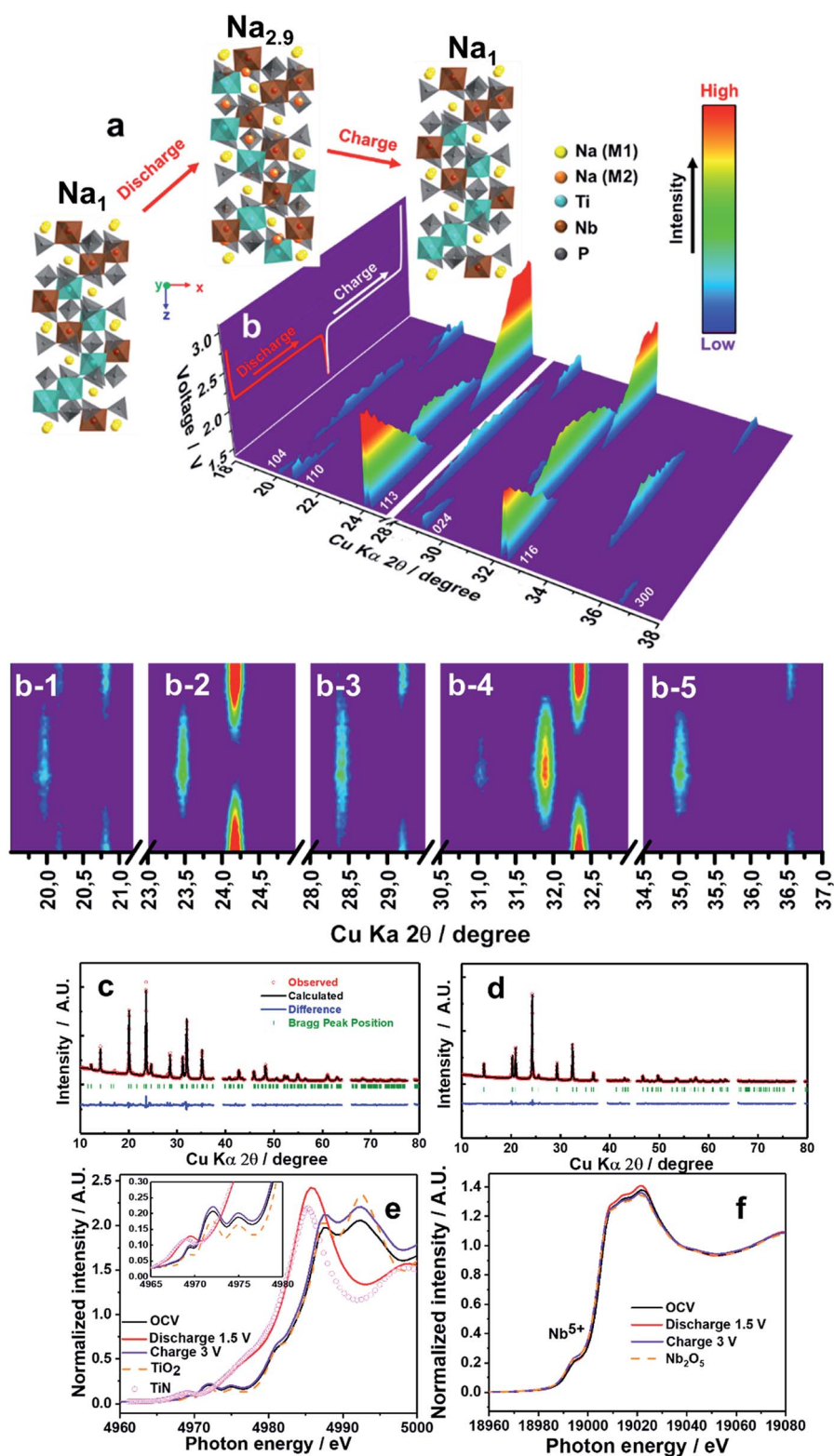


Fig. 4 (a) Schematic illustration of the unit cell of NNbTP-C during discharge/charge in the voltage range of 1.5–3 V. (b) 3D *operando* XRD patterns of the NNbTP-C electrode recorded during discharge/charge of the first cycle in the voltage range of 1.5–3 V in the 2θ range of 18° to 38° (c) Rietveld refinement results of XRD data for the NNbTP-C electrode (c) discharged to 1.5 V and (d) charged to 3 V. (e) XANES K-edge spectra of Ti (the inset compares the pre-edge with that of several titanium compounds). (f) XANES K-edge spectra of Nb for the electrode discharged to 1.5 V and charged to 3 V.

refinement results of the electrode charged to 3 V (Fig. 4d and Table S2, ESI†).

The K-edge spectra of Ti and Nb were used to follow the variation in the oxidation states of Ti and Nb in NNbTP in the voltage range of 1.5–3 V. The XANES spectrum of the fresh NNbTP-C electrode was similar to that of anatase TiO₂, including the pre-edge region (Fig. 4e), which indicates that the oxidation state of Ti is tetravalent. As the cell was discharged to 1.5 V, the main peak shifted toward the lower-photon-energy direction because of the decrease in the Ti oxidation state. A similar tendency was also observed in the pre-edge; specifically, the related pre-edge spectrum was close to that of the Ti³⁺N reference. Again, charging to 3 V resulted in the spectrum shifting back to higher photon energy, where even the pre-edge spectrum was identical to that of the fresh state of the NNbTP electrode. Unlike the reversible variation in the oxidation state of Ti, there were no changes in the oxidation state of Nb on discharging and charging (Fig. 4f). It is thought that Nb does not participate in the electrochemical reaction but supports the crystal structure stability during sodiation and desodiation in the range of 1.5–3 V.

Sodium insertion and extraction into/from Na_{2.9}Nb_{0.05}Ti_{1.95}(PO₄)₃-C (0.01–1.5 V)

To further investigate the sodium insertion into NNbTP-C, *operando* XRD measurements were performed in the voltage range of 0.01–1.5 V (Fig. 5a and b). Reduction of Na_{2.9}Nb_{0.05}Ti_{1.95}(PO₄)₃ resulted in the gradual growth of new peaks at 19.6°, 23.4°, 28.2°, 31.2°, 31.3°, and 34.8° (2θ) when sodiated to Na_{3.4}Nb_{0.05}Ti_{1.95}(PO₄)₃ at approximately 0.41 V, which is the intermediate point between the upper step (0.43 V) and the lower step (0.39 V) on the low-voltage plateau, showing a downslope. Surprisingly, these peaks gradually shifted toward the lower angle in this short sloppy voltage variation range between 0.43 and 0.39 V. Later, these peaks further converted into those of the newly developed single phase of Na_{3.875}Nb_{0.05}Ti_{1.95}(PO₄)₃ with diffraction peaks at 20.1°, 23.3°, 28.2°, 30.5°, 32.0°, and 34.4° (2θ). Compared with the earlier work by Palacin *et al.*¹³ indicating that the reaction occurred *via* one biphasic reaction, the present phase evolution from Na_{2.9}Nb_{0.05}Ti_{1.95}(PO₄)₃ to Na_{3.875}Nb_{0.05}Ti_{1.95}(PO₄)₃ clearly consists of two types of biphasic reactions upon discharge in the voltage range of 0.01–1.5 V, as demonstrated by the two distinct plateaus at 0.43 and 0.39 V in the dQ/dV curve on discharge (Fig. 2b). Notably, the capacities delivered at the two plateaus at 0.43 and 0.39 V are almost equal, implying the presence of an intermediate phase, Na_{3.4}Nb_{0.05}Ti_{1.95}(PO₄)₃, between the two terminal phases of Na_{2.9}Nb_{0.05}Ti_{1.95}(PO₄)₃ and Na_{3.875}Nb_{0.05}Ti_{1.95}(PO₄)₃. The peaks at 19.6°, 23.4°, 28.2°, 31.1°, 31.3°, and 34.8° (2θ) are thus attributed to the intermediate phase of Na_{3.4}Nb_{0.05}Ti_{1.95}(PO₄)₃. The unit cell parameters of the terminal Na_{3.875}Nb_{0.05}Ti_{1.95}(PO₄)₃ with the R3C space group were retrieved from the *operando* XRD data of the NNbTP-C electrode discharged to 0.01 V (Fig. 5c and Table S2, ESI†). Rietveld refinement of the Na_{3.875}Nb_{0.05}Ti_{1.95}(PO₄)₃ revealed the variation in the unit volume of approximately 3.17% compared with

that of Na_{2.9}Nb_{0.05}Ti_{1.95}(PO₄)₃ when the electrode was charged to 1.5 V (Fig. 5d and Table S2, ESI†). This volume change is roughly half of that for the 1.95 mol insertion of Na⁺ into Na_{2.9}Nb_{0.05}Ti_{1.95}(PO₄)₃, which is tolerable for Na⁺ insertion and extraction throughout long-term cycles.

During charge, the peaks of Na_{3.875}Nb_{0.05}Ti_{1.95}(PO₄)₃ started to disappear and coexist with Na_{3.4}Nb_{0.05}Ti_{1.95}(PO₄)₃ peaks, which were then converted to those of the Na_{2.9}Nb_{0.05}Ti_{1.95}(PO₄)₃ phase (Fig. 5b). The intensity of the peaks of the intermediate Na_{3.4}Nb_{0.05}Ti_{1.95}(PO₄)₃ phase was weaker on charge than on discharge (Fig. 5b–4), which is consistent with the galvanostatic data, where the voltage step almost disappeared at ~0.4 V.

Notably, the *operando* XRD study revealed that the structural change is highly reversible during the charge–discharge process in the low voltage region between 0.01 and 1.5 V. To validate the change of the valence state of Ti and Nb in the lower voltage region, XANES was employed upon sodiation to 0.01 V. It is clear that Ti K-edge spectra shifted to lower binding energy, indicating the tendency of decreasing of the average oxidation state of Ti during sodiation upon 0.01 V (Fig. 5e). The pre-edge of Ti at 0.01 V showed a mixed valence state of Ti³⁺ and Ti²⁺ because the adsorption edge energy of the electrode was lower than that of Ti³⁺N, but higher than that of Ti²⁺O. During charge, energy positions of Ti K-edge XANES spectra reversibly shifted back toward higher energy regions (Fig. 5e). On the contrary, Nb K-edge XANES spectra displayed no change in the pre-edge and white lines, indicating that the Nb⁵⁺ valence did not vary after the cell was completely discharged to 0.01 V and charged back to 1.5 V (Fig. 5f).

The Rietveld refinement and XANES results indicate that the delivered reversible capacity of 64 mA h g⁻¹ resulted from the redox reaction of Ti^{3+/2+} attributed to 0.975 Na⁺ intercalation. In contrast, the capacity determined from galvanostatic measurements of NNbTP-C in the low-voltage range was 86 mA h g⁻¹ (Fig. 3e). This discrepancy arises from the capacity contribution of the amorphous carbon added as a conducting agent or coated carbon product in the low-voltage range of 0–1.5 V. Indeed, amorphous carbon materials, such as Super P and pitch carbon, can store Na⁺ ions with high reversible capacities.^{44,45} Therefore, the electrode prepared with the same conductive additive ratio as in NTP-C and NNbTP-C electrodes (Super P : pitch carbon = 2 : 1) contributed to a reversible capacity of ~23 mA h g⁻¹ (Fig. S5, ESI†). The remaining capacity of 63 mA h g⁻¹ for NNbTP-C agrees well with the Rietveld refinement results and XANES data.

Consequently, the structural evolution of Nb⁵⁺-doped NaNb_{0.05}Ti_{1.95}(PO₄)₃ agrees well with that of undoped NaTi₂(PO₄)₃ (Fig. S6 and Table S2, ESI†) and previous reports on phase transition in the NTP structure,^{12,13} indicating that Nb⁵⁺ doping of NaTi₂(PO₄)₃ does not have any harmful effects on the structure or electrochemical performance. Specifically, Nb⁵⁺ doping improves the Na-ion reaction kinetics compared with that of undoped NTP. This enhancement was clearly confirmed by the low polarization in the GITT data (Fig. 2c), increased electrical conductivity measured using the direct volt–ampere method (Table S1, ESI†), and impedance measurements (Fig. S7, ESI†).

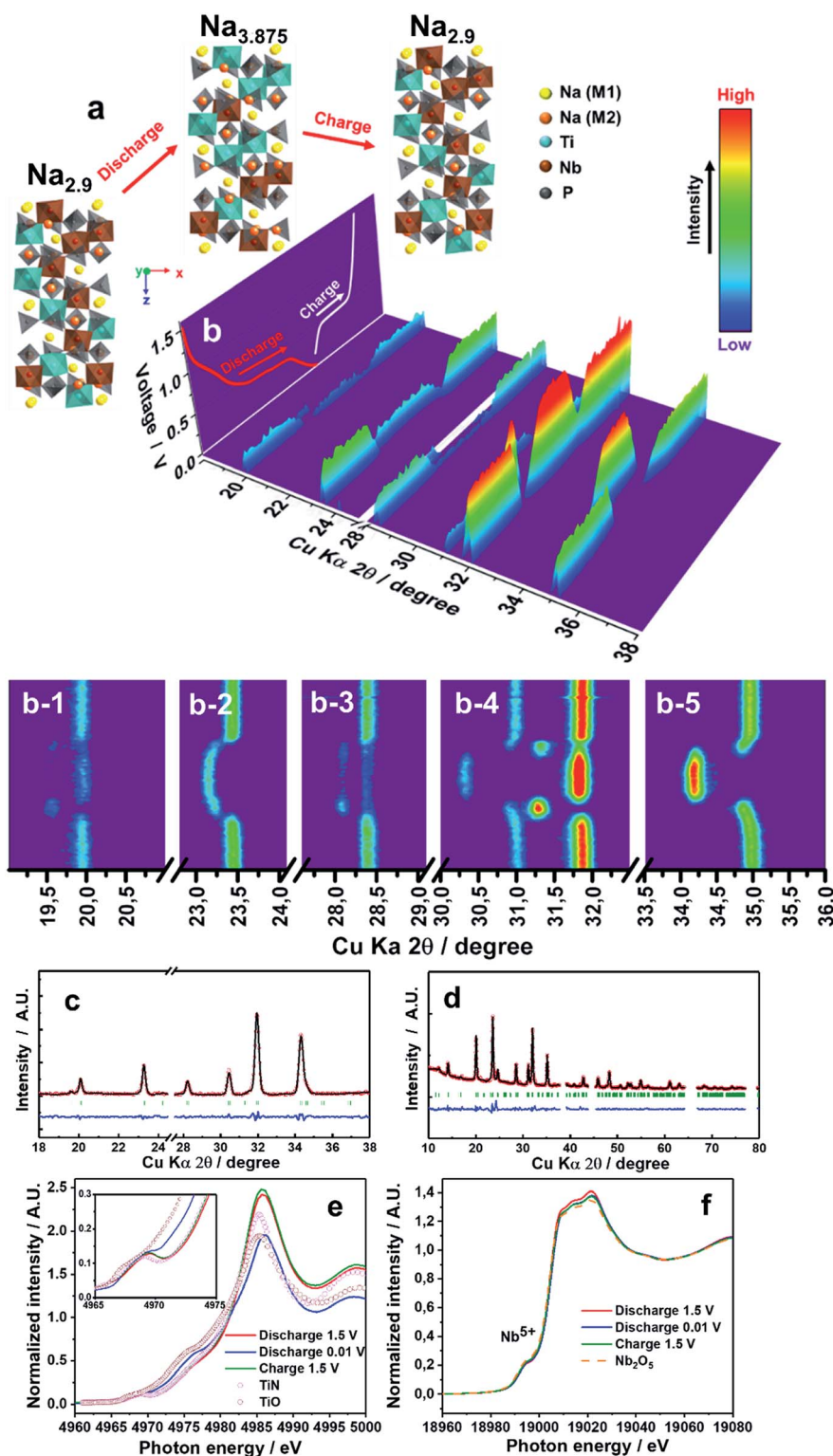


Fig. 5 (a) Schematic illustration of the unit cell of NNbTP-C during discharge/charge in the voltage range of 0.01–1.5 V. (b) 3D *operando* XRD patterns of the NNbTP-C electrode recorded during discharge/charge of the first cycle in the voltage range of 0.01–1.5 V in the 2θ range of 18° to 38° . (c) Rietveld refinement results of XRD data for the NNbTP-C electrode (c) discharged to 0.01 V and (d) charged to 1.5 V. (e) XANES K-edge spectra of Ti (the inset compares the pre-edge with that of several titanium compounds) and (f) XANES K-edge spectra of Nb for the electrode discharged to 0.01 V and charged to 1.5 V.

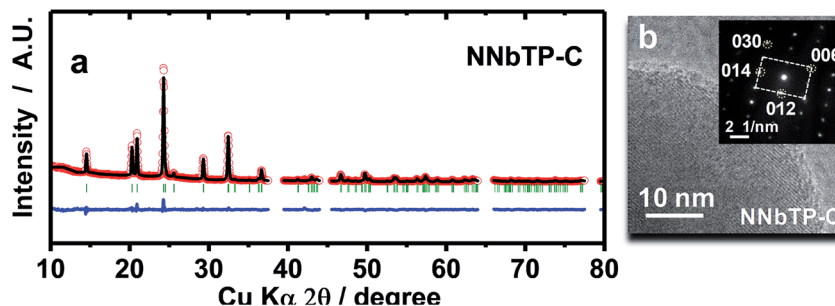


Fig. 6 (a) Rietveld refinement results of XRD data for NNbTP-C electrodes after 1000 cycles charged to 3 V. (b) TEM image and the corresponding SAED pattern along the [100] zone axis of NNbTP-C.

Post cycle analysis of electrodes

To prove the structural stabilities of NTP-C and NNbTP-C during long-term cycling, Rietveld refinement of the XRD data was performed and TEM images with SAED patterns were obtained after 1000 cycles (Fig. 6 and S8, ESI†). No obvious structural changes were observed in the Rietveld refinement data (Fig. 6a, S8a and Table S3, ESI†). The lattice parameters remained almost constant after 1000 cycles for both the NNbTP-C and NTP-C electrodes. The corresponding SAED patterns along the [100] zone axis of NNbTP-C and NTP-C were also identical, indicating the excellent structural stability of both materials during cycling (Fig. 6b and S8b, ESI†).

Symmetric battery

In summary, the natural multi-step redox reaction of Ti enabled the assembly and testing of a symmetric NNbTP/NNbTP SIB, which demonstrated the practicality of simultaneously using the prepared NNbTP-C as both a cathode and an anode in SIBs (Fig. 7a). Prior to symmetric cell fabrication, the full pre-sodiation of the NNbTP-C anode was performed to alleviate the irreversible capacity of the amorphous carbon. The cell balance was achieved by setting the cathode/anode mass ratio to 0.6 (the cathode loading mass is approximately 1.5 mg cm^{-2}).

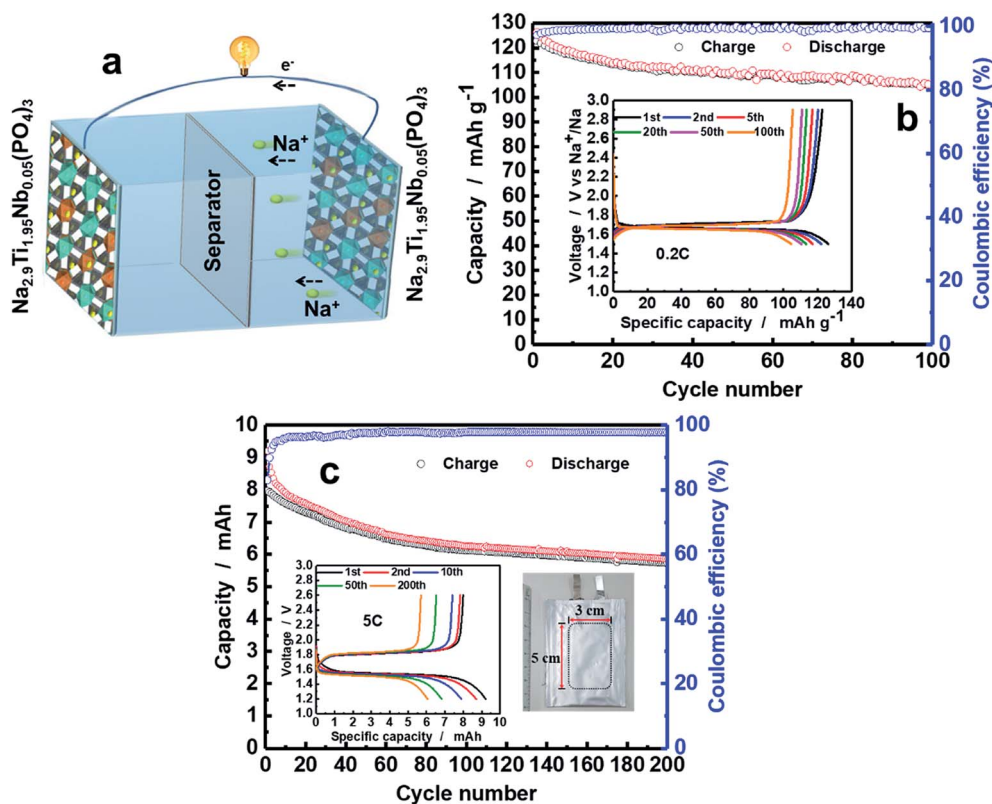


Fig. 7 (a) Schematic illustration of the symmetric NNbTP cell design. (b) Cycling performance of the symmetric NNbTP/NNbTP cell and coulombic efficiency at 0.2C (inset: charge/discharge curves in the voltage range of 1.5–2.8 V). (c) Cycling performance of the symmetric pouch NNbTP/NNbTP cell and coulombic efficiency at 5C (inset: charge/discharge curves in the voltage range of 1.2–2.6 V and a digital photo of the symmetric pouch cell).

The average potential of the symmetric cell was approximately 1.7 V, with a single voltage plateau and an initial discharge capacity of 126 mA h g⁻¹ based on the mass of the cathode. As observed in the inset of Fig. 7b, the charge-discharge profiles exhibited symmetric characteristics with no obvious polarization in this symmetric cell configuration. The cell delivered a capacity of 105 mA h g⁻¹, reaching 83% capacity retention over 100 cycles at 0.2C (Fig. 7b).

To examine the industrial applicability of the NNbTP-C material, a symmetric pouch full cell was manufactured. It should be noted that the cell was cycled at a quite rapid discharge/charge rate of 5C to investigate the cycling ability. In Fig. 7c, the corresponding discharge/charge curves and cycling performance are presented. The symmetric pouch cell showed very stable retention characteristics during 200 cycles (65%). Therefore, the efficiency of the symmetric cell based on NNbTP-C electrodes confirmed the stability of the material at low and high working potentials, thereby proving the potential of this material in practical applications.

Conclusions

To improve the cycling performance of NaTi₂(PO₄)₃, Nb⁵⁺-doped carbon-coated NaNb_{0.05}Ti_{1.95}(PO₄)₃ materials were prepared. The electronic conductivity associated with the lowered band gap energy of NaNb_{0.05}Ti_{1.95}(PO₄)₃ was significantly improved after the dual treatment of Nb⁵⁺ doping and carbon coating. This improved electronic conductivity was beneficial for facile electron transfer, thereby improving the electrode performance. Combined *operando* XRD and XANES investigations revealed that the reversible structural evolution accompanying Na⁺ insertion and extraction occurred *via* a biphasic redox mechanism involving Ti^{4+/3+} and Ti^{3+/2+} redox pairs, which enabled the operation of symmetric cells with stable cycle performance (capacity retention exceeding 83% over 100 cycles). Our findings demonstrate that doping with aliovalent metal ions is an efficient strategy to optimize NASICON-structured materials as high-rate and stable electrode materials for SIBs.

Conflicts of interest

There are no conflicts to declare.

Acknowledgements

This research was supported by the Basic Science Research Program through the National Research Foundation of Korea (NRF), and funded by the Ministry of Education, Science, and Technology of Korea (NRF 2017K1A3A1A30084795, NRF 2017R1E1A2A01079404, 2017M2A2A6A01070834 and NRF 2015M3D1A1069713). The calculation resources were supported by the Supercomputing Center in Korea Institute of Science and Technology Information (KSC-2018-C2-0034).

References

- 1 S. Guo, J. Yi, Y. Sun and H. Zhou, *Energy Environ. Sci.*, 2016, **9**, 2978.
- 2 J.-Y. Hwang, S.-T. Myung and Y.-K. Sun, *Chem. Soc. Rev.*, 2017, **46**, 3529.
- 3 Y. Mei, Y. Huang and X. Hu, *J. Mater. Chem. A*, 2016, **4**, 12001.
- 4 K.-T. Kim, C.-Y. Yu, S.-J. Kim, Y.-K. Sun and S.-T. Myung, *Nano Energy*, 2015, **12**, 725.
- 5 J.-Y. Hwang, S.-T. Myung, J.-H. Lee, A. Abouimrane, I. Belharouak and Y.-K. Sun, *Nano Energy*, 2015, **16**, 218.
- 6 D. Wang, X. Bie, Q. Fu, D. Dixon, N. Bramnik, Y.-S. Hu, F. Fauth, Y. Wei, H. Ehrenberg, G. Chen and F. Du, *Nat. Commun.*, 2017, **8**, 15888.
- 7 Z. Zhang, M. Li, Y. Gao, Z. Wei, M. Zhang, C. Wang, Y. Zeng, B. Zou, G. Chen and F. Du, *Adv. Funct. Mater.*, 2018, **28**, 1802684.
- 8 Z. Wei, D. Wang, M. Li, Y. Gao, C. Wang, G. Chen and F. Du, *Adv. Energy Mater.*, 2018, **8**, 1801102.
- 9 H. Yoshida, N. Yabuuchi, K. Kubota, I. Ikeuchi, A. Garsuch, M. Schulz-Dobrick and S. Komaba, *Chem. Commun.*, 2014, **50**, 3677.
- 10 P.-F. Wang, H.-R. Yao, X.-Y. Liu, Y.-X. Yin, J.-N. Zhang, Y. Wen, X. Yu, L. Gu and Y.-G. Guo, *Sci. Adv.*, 2018, **4**(3), eaar6018.
- 11 M. H. Han, E. Gonzalo, N. Sharma, J. M. López del Amo, M. Armand, M. Avdeev, J. J. S. Garitaonandia and T. Rojo, *Chem. Mater.*, 2016, **28**, 106.
- 12 C. Delmas, F. Cherkaoui, A. Nadiri and P. Hagemmuller, *Mater. Res. Bull.*, 1987, **22**, 631.
- 13 P. Senguttuvan, G. Rousse, M. E. Arroyo y de Dompablo, H. Vezin, J.-M. Tarascon and M. R. Palacin, *J. Am. Chem. Soc.*, 2013, **135**, 3897.
- 14 X. Lu, S. Wang, R. Xiao, S. Shi, H. Li and L. Chen, *Nano Energy*, 2017, **41**, 626.
- 15 J. Song, S. Park, J. Gim, V. Mathew, S. Kim, J. Jo, S. Kim and J. Kim, *J. Mater. Chem. A*, 2016, **4**, 7815.
- 16 Y. Jiang, J. Shi, M. Wang, L. Zeng, L. Gu and Y. Yu, *ACS Appl. Mater. Interfaces*, 2016, **8**, 689.
- 17 Y. Fang, L. Xiao, J. Qian, Y. Cao, X. Ai, Y. Huang and H. Yang, *Adv. Energy Mater.*, 2016, **6**(19), 1502197.
- 18 G. Xu, L. Yang, Z. Li, X. Wei and P. K. Chu, *J. Mater. Chem. A*, 2017, **5**, 2749.
- 19 P. Wei, Y. Liu, Z. Wang, Y. Huang, Y. Jin, Y. Liu, S. Sun, Y. Qiu, J. Peng, Y. Xu, X. Sun, C. Fang, J. Han and Y. Huang, *ACS Appl. Mater. Interfaces*, 2018, **10**, 27039.
- 20 D. Wang, Q. Liu, C. Chen, M. Li, X. Meng, X. Bie, Y. Wei, Y. Huang, F. Du, C. Wang and G. Chen, *ACS Appl. Mater. Interfaces*, 2016, **8**, 2238.
- 21 C. Xu, Y. Xu, C. Tang, Q. Wei, J. Meng, L. Huang, L. Zhou, G. Zhang, L. He and L. Mai, *Nano Energy*, 2016, **28**, 224.
- 22 B. Tian, H. Xiang, L. Zhang, Z. Li and H. Wang, *Electrochim. Acta*, 2010, **55**, 5453.
- 23 M. Guo, S. Wang, L.-X. Ding, C. Huang and H. Wang, *J. Power Sources*, 2015, **283**, 372.
- 24 F. Zhao, B. Wang, Y. Tang, H. Ge, Z. Huang and H. K. Liu, *J. Mater. Chem. A*, 2015, **3**, 22969.
- 25 S.-T. Myung, M. Kikuchi, C. S. Yoon, H. Yashiro, S.-J. Kim, Y.-K. Sun and B. Scrosati, *Energy Environ. Sci.*, 2013, **6**, 2609.
- 26 J.-S. Park, J. Kim, J. H. Jo and S.-T. Myung, *J. Mater. Chem. A*, 2018, **6**, 16627.

- 27 W. Shen, H. Li, Z. Guo, Z. Li, Q. Xu, H. Liu and Y. Wang, *RSC Adv.*, 2016, **6**, 71581.
- 28 X. Li, Y. Huang, J. Wang, L. Miao, Y. Li, Y. Liu, Y. Qiu, C. Fang, J. Han and Y. Huang, *J. Mater. Chem. A*, 2018, **6**, 1390.
- 29 M. J. Aragón, P. Lavela, G. F. Ortiz and J. L. Tirado, *ChemElectroChem*, 2015, **2**(7), 995.
- 30 J.-S. Park, J. Kim, W. B. Park, Y.-K. Sun and S.-T. Myung, *ACS Appl. Mater. Interfaces*, 2017, **9**, 40307.
- 31 H.-B. Sun, L.-L. Zhang, X.-L. Yang, G. Liang and Z. Li, *Dalton Trans.*, 2016, **45**, 15317.
- 32 M. Ren, Z. Zhou, Y. Li, Y. Li, X. P. Gao and J. Yan, *J. Power Sources*, 2006, **162**, 1357.
- 33 M. J. Aragón, C. Vidal-Abarca, P. Lavela and J. L. Tirado, *J. Power Sources*, 2014, **252**, 208.
- 34 F. E. Mouahid, M. Bettach, M. Zahir, P. Maldonado-Manso, S. Bruque, E. R. Losilla and M. A. G. Aranda, *J. Mater. Chem.*, 2000, **10**, 2748.
- 35 Z. Huang, M. Yao, Z. Jiang, W. Meng, B. Li, C. Li, C. Li, Z. He, W. Meng, L. Dai and L. Wang, *Solid State Ionics*, 2018, **327**, 123.
- 36 O. Tillement, J. Angenault, J. C. Couturier and M. Quarton, *Solid State Ionics*, 1992, **53–56**, 391.
- 37 T. Roisnel and J. Rodriguez-Carjaval, *Fullprof Manual*, Institut Laue-Langevin, Grenoble, France, 2002.
- 38 B. Ravel and M. Newville, Athena, Artemis, Hephaestus, *J. Synchrotron Radiat.*, 2005, **12**, 537.
- 39 J. P. Perdew, K. Burke and M. Ernzerhof, *Phys. Rev. Lett.*, 1996, **77**, 3865.
- 40 P. E. Blöchl, *Phys. Rev. B: Condens. Matter Mater. Phys.*, 1994, **50**, 17953.
- 41 G. Kresse and J. Furthmüller, *Comput. Mater. Sci.*, 1996, **6**, 15.
- 42 V. I. Anisimov, J. Zaanen and O. K. Andersen, *Phys. Rev. B: Condens. Matter Mater. Phys.*, 1991, **44**, 943.
- 43 B. J. Morgan, D. O. Scanlon and G. W. Watson, *J. Mater. Chem.*, 2009, **19**, 5175.
- 44 C.-M. Wu, P.-I. Pan, Y.-W. Cheng, C.-P. Liu, C.-C. Chang, M. Avdeev and S.-K. Lin, *J. Power Sources*, 2017, **340**, 14.
- 45 Y. Li, Y.-S. Hu, H. Li, L. Chen and X. Huang, *J. Mater. Chem. A*, 2016, **4**, 96–104.